International Journal of Solids and Structures 106–107 (2017) 305–314

Contents lists available at ScienceDirect

International Journal of Solids and Structures

journal homepage: www.elsevier.com/locate/ijsolstr

Experimental and numerical analysis of the Lüders phenomenon in simple shear

M. Mazière[a,*], C. Luis[b], A. Marais[a], S. Forest[a], M. Gaspérini[b]

[a] Mines ParisTech, Centre des Matériaux, CNRS UMR7633, BP 87, 91003 Evry cedex, France
[b] Université Paris 13, Sorbonne Paris Cité, Laboratoire des Sciences des Procédés et des Matériaux (LSPM), CNRS(UPR3407), 99 av. J.B. Clément, F-93430 Villetaneuse, France

ARTICLE INFO

Article history:
Received 2 September 2015
Revised 4 July 2016
Available online 3 September 2016

Keywords:
Lüders phenomenon
Shear experiment
Static-strain ageing
Strain gradient plasticity model

ABSTRACT

The Lüders phenomenon is investigated in a low carbon ferritic steel under simple shear loading. Tensile and shear experiments are carried out associated with digital image correlation (DIC) measurements of the local strain field. An elastoviscoplastic constitutive law is identified with special attention paid to the choice of the equivalent stress measure in the yield function. It is then used to simulate the shear experiment using finite element analyses. Several mesh types and sizes are used to illustrate some mesh sensitivity observed in the finite element results. A regularized model based on strain gradient plasticity is then proposed to ensure fully mesh insensitive simulations and properly describe the finite thickness of the Lüders band front. The additional internal length introduced in the regularized model is identified from the DIC strain measurements. Finally, the boundary conditions best–suited for an accurate description of the shear experiment are discussed.

1. Introduction

The well known peak stress and Lüders plateau that are observed on the tensile curves of some metallic materials at the elastic to plastic transition have been experimentally evidenced in the 19th century by Piobert (1842) and Lüders (1860). These particular phenomena have been attributed by Cottrell and Bilby (1949) to the pinning of mobile dislocations by solute atoms in the metal crystal lattice. This interaction of dislocations with solute atoms is called strain ageing. If an ageing thermal treatment is carried out on a metallic specimen, solute atoms can diffuse close to dislocations. Compared with a non-aged material, a higher stress level is required to trigger plastic deformation. This phenomenon has been mainly studied under tensile loading conditions (Ballarin et al., 2009; Hallai and Kyriakides, 2013; Kyriakides and Miller, 2000; Lomer, 1952; Marais et al., 2012), but also in the case of bending of tubes (Aguirre et al., 2004; Hallai and Kyriakides, 2011a; 2011b; Kyriakides et al., 2008), torsion of cylindrical specimens (Elliot et al., 2004), or combined tension/torsion (Zhang and Jiang, 2005). Its influence on brittle and ductile failure of steels has been investigated using CT (Amar and Pineau, 1985; Wenman and Chard-Tuckey, 2010) or Charpy specimens (Marais et al., 2015). More recently Lüders and Portevin - Le Chatelier phenomena have also been investigated from an experimental and numerical point of view during a shear test on flat specimens in the case of a Al-Mg alloy (Coer et al., 2013; Manach et al., 2014). For all these loading conditions, when the peak force stress is reached, the unpinning process of dislocations induces a softening of the material followed by the propagation of one or several bands of plastic deformation all along the specimen's gauge length.

Coer et al. (2013) experimentally evidenced strain heterogeneities development during simple shear at room temperature of an AA5754 aluminum alloy using the DIC technique. Strain and strain rate mapping in the sample gauge length permitted to characterize the strain banding responsible for the Piobert-Lüders plateau at the beginning of the test and for strain-rate dependent PLC phenomena with serrations on the tensile curves at larger strains. The observed phenomena were qualitatively consistent with strain ageing phenomena during tensile testing, however it can be noticed that the so-called Piobert-Lüders plateau in this alloy was not preceded by a peak stress, contrary to the well-known tensile curves for low carbon steels (Marais et al., 2012). In a more recent paper (Manach et al., 2014), the kinematics of the PLC bands in simple shear at different temperatures and strain-rates was studied experimentally and finite element (FE) simulations of the test were presented. Models by McCormick (1988) and Johnson and Cook (1985) were used in the simulations. The von Mises yield potential was used despite the observed discrepancy between model and experiment when com-

* Corresponding author. Fax: +33160763000.
E-mail address: matthieu.maziere@mines-paristech.fr (M. Mazière).

http://dx.doi.org/10.1016/j.ijsolstr.2016.07.026
0020-7683/

paring the tensile and shear responses. Moreover, as FE mesh sensitivity in the simulations of strain localization phenomena was noticed by Manach et al. (2014), only qualitative agreement with experiment could be reaching, pointing out the need for regularization methods to improve the reliability of the simulations.

The issue of mesh sensitivity of finite element simulation results of Lüders banding has been discussed in some recent publications (Liu et al., 2015; Manach et al., 2014; Mazière et al., 2010; Mazière and Forest, 2015). Even though reliable results can be obtained in many situations of Lüders banding simulations, as illustrated for instance by the recent simulations in the latter reference, spurious effects are observed in the worst case, i.e. for a regular mesh and when the band front is parallel to the element edges (Marais et al., 2012; Mazière and Forest, 2015). In this particular case it has been observed for 2D (Marais et al., 2012) and 3D (Mazière and Forest, 2015) simulations that the band front size reduces to one single row of elements and is consequently highly mesh dependent. There are essentially two methods of regularizing the problem: In method I, it is achieved by the introduction of some rate dependence to the problem. In method II regularization is obtained by the introduction of higher order gradients to the formulation. The choice of the method depends in fact on the available experimental information. For the steel considered by Marais et al. (2012) in the present work, the actual viscosity parameters are identified from tests at various strain rates. The viscosity was found in Marais et al. (2012) to be not sufficient to regularize the problem. It follows that the method I cannot be used any more because the viscosity is known and the corresponding parameters cannot be modified. Strain gradient plasticity was used by Marais et al. (2012) and Mazière and Forest (2015) in the case of Lüders band formation and propagation in tension. This requires the introduction of a characteristic length that can be identified using DIC field measurements. Indeed, the recent developments of strain fields measurements by DIC permit to characterize accurately the local features of Lüders and Portevin - Le Chatelier bands (Marais et al., 2012; Nogueira de Codes et al., 2011; Wattrisse et al., 2001). The introduction of strain gradient plasticity then serves two objectives: (i) to ensure strictly mesh–independent finite element results and (ii) to account for the physical reality of finite size Lüders band fronts.

In this context, the aim of the present study is to develop an experimental and numerical analysis of the Lüders phenomenon during simple shear, based on experimental investigations on a thin sheet of ultra-low carbon steel. Special attention is paid to the choice of the plasticity yield potential, and a strain gradient plasticity model is used to overcome the inherent mesh sensitivity of localized strain fields in finite element simulations. The determination of the characteristic length is based on experimental results of mechanical testing and strain fields measurements.

The paper is organized as follows. In Section 2, the experimental results are presented including shear and tensile curves and DIC strain field measures. In Section 3, the material model proposed to simulate experimental results is described, together with the material parameter identification procedure. In Section 4, the simulations of shear test are detailed in three steps: (i) evidence of some mesh sensitivity of the FE results, (ii) regularisation of the model and identification of the internal length using DIC experimental measurements, (iii) improvement of the boundary conditions for more realistic simulations.

2. Experimental observations

2.1. Material

Ultra low carbon (1.9×10^{-3} C wt%) ferritic steel for packaging was used for the study. The material was provided as thin sheets,

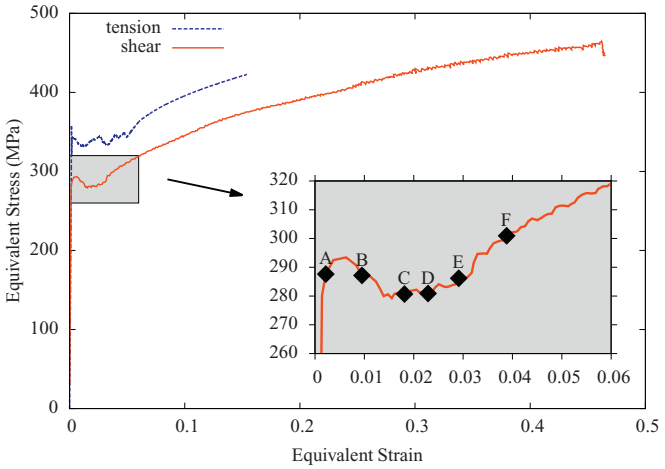

Fig. 1. Evolution of the equivalent stress vs. equivalent strain for tensile and shear experiments at room temperature. The equivalent stress and strain are calculated from the stress and strain tensors using the usual von Mises norms. DIC measurements have been performed at the points indicated by markers.

obtained by cold-rolling and annealing, followed by 2.5% thickness reduction by temper-rolling and final ageing treatment at 200 °C for 20 mn. The sheet thickness was $t = 0.24$ mm.

2.2. Tensile and shear tests

Simple (planar) shear testing along the rolling direction was performed on a home-made device mounted on a conventional tensile machine (Bouvier et al., 2006). Rectangular samples of length L = 30 mm, width w = 18 mm and thickness t were cut from the sheet, the dimensions of the sheared zone being $L \times b \times t$ with $b = 2$ mm to ensure quasi-uniform straining in the absence of strain ageing phenomena. The tests were conducted under constant shear strain rate $\dot{\gamma} = \sqrt{3} \times 10^{-3} s^{-1}$ thanks to the control by video-extensometry of the average inclination of a black line initially drawn on the sample surface at the center of the sheared zone perpendicularly to the shear direction. One face of the sample was covered by a thin speckle obtained by airbrush, permitting to get the strain fields in the narrow sheared zone by DIC method using Aramis© system. For DIC measurements, pictures with size 2448 × 2050 pixels were taken by the camera of the non-contact measuring system (Aramis 5M, Gom, Germany) at 0.8 pictures/s. Due to the large aspect ratio of the sheared zone (30:2) compared to the recorded pictures, the width of the shear zone was about 140 pixels, i.e. 70 px/mm. DIC measurements were made with a virtual grid 15 × 15 px and a 7 px step. The shear stress τ was computed as $\tau = F/(Lt)$, where F is the cell load acting on the shear sample. The shear strain γ-shear stress τ curve was converted into equivalent von Mises stress - equivalent strain curve with $\sigma = \sqrt{3}\tau$ and $\varepsilon = \gamma/\sqrt{3}$. Comparison with standard tensile test is shown on Fig. 1. As expected, due to the absence of necking, larger strains are reached during shear tests. The discrepancy between the two curves shows that the von Mises yield potential is not appropriate to describe the material behaviour along both loading paths. More complex plastic potentials have been developed for anisotropic rolled sheets, as reviewed in Rabahallah et al. (2009). However, they may involve a huge number of parameters and are sensitive to the identification procedure. In the present case, for the sake of simplicity, as the stress-strain curves and the observed Lüders phenomena are not significantly dependent on the direction of testing (see Luis, 2011; Luis et al., 2009), only the consistency of plastic yielding for shear and tensile tests is accounting for, using a Hosford cri-

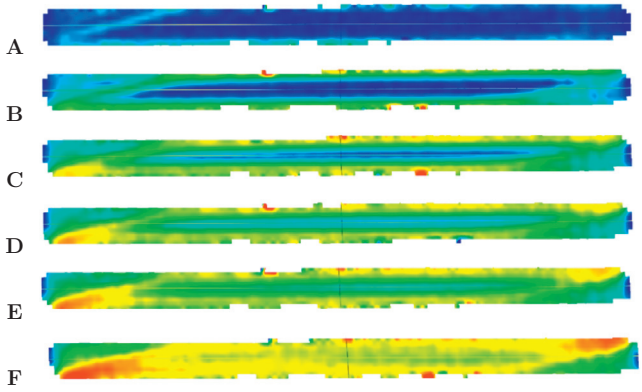

Fig. 2. Map of the shear strain ε_{12} (blue 0%, red 5%) given by digital image correlation method on the experiment presented on Fig. 1. The vertical straight line is used to extract the evolution of shear strain along the vertical axis as plotted on Fig. 3. (For interpretation of the references to colour in this figure legend, the reader is referred to the web version of this article.)

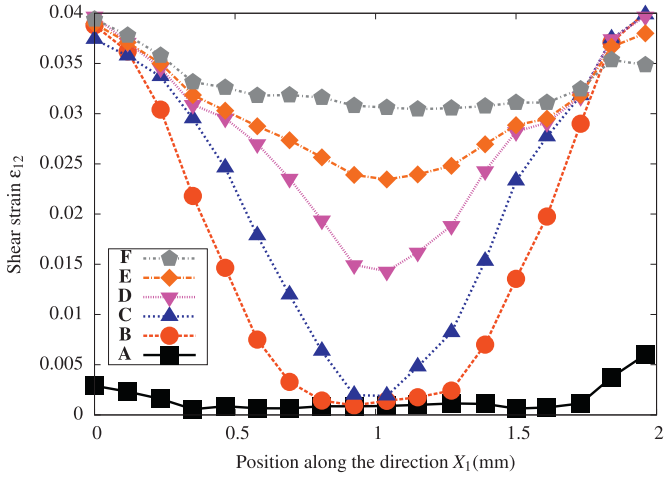

Fig. 3. Evolution of the shear strain ε_{12} along a line located at the centre of the specimen (see Fig. 2) for the six strain levels marked on the shear curve of Fig. 1. (For interpretation of the references to colour in this figure legend, the reader is referred to the web version of this article.)

terion (Hosford, 1972) needing only one extra parameter to adjust the yield surface shape.

2.3. Lüders bands

Lüders bands are observed during the shear test at the beginning of plastic yielding, in the approximate range 0.3% - 6% for the average shear strain γ, as illustrated by the measured map of ε_{12} $(=\gamma/2)$ component in Fig. 2. Two symmetric bands are clearly visible along the sample grips in a large part of the sheared zone, progressing towards the sample center with increasing overall strain, and remain parallel to the direction of shear. The bands join together close to the sample free ends, where the band fronts deviate from the direction of shear, consistently with compressive stress acting in this zone. The mechanism is quite different than the one observed by Coer et al. (2013) in a Al-Mg alloy where a single band nucleates at one side of the specimen and propagates all along.

The Fig. 3 shows the ε_{12} shear strain profile evolution in the middle of the sheared zone, along a virtual line initially perpendicular to the shear direction. The correspondence between profiles and overall strain on the shear curve is indicated by markers on Fig. 1. Once the strain becomes homogeneous throughout the sheared zone (except unavoidable free end effects), the stress-strain curve displays the usual strain-hardening behavior.

3. Material model

3.1. Constitutive equations

The simulation of strain ageing requires a suitable elasto-viscoplasticity model including the physical mechanisms of pinning and unpinning of dislocations. The model retained in this work and initially proposed by Kubin and Estrin (1985) and McCormick (1988) and modified by Graff et al. (2004) is based on the introduction of an internal variable t_a called ageing time with an evolution law coupled with plastic flow. It has been implemented in the finite element code Zset and used in several previous studies (Belotteau et al., 2009; Mazière et al., 2010; Mazière and Dierke, 2012; Wang et al., 2012). For more details about the model, its implementation and the identification process, the reader is referred to Marais et al. (2012).

A finite strain formulation for isotropic nonlinear material behavior is adopted in this work based on the concept of local objective frame as proposed in Sidoroff and Dogui (2001), Bertram (2005) and Besson et al. (2009). Observer invariant stress and strain rate measures $\underset{\sim}{\sigma}$ and $\underset{\sim}{\dot{\varepsilon}}$ are defined by transport of the Cauchy stress tensor $\underset{\sim}{T}$ and the strain rate tensor $\underset{\sim}{D}$ into the corotational frame characterized by the rotation $\underset{\sim}{Q}(\underline{x},t)$. This change of frame takes place at each material point :

$$\begin{cases} \underset{\sim}{\sigma} = \underset{\sim}{Q}.\underset{\sim}{T}.\underset{\sim}{Q}^{T} \\ \underset{\sim}{\dot{\varepsilon}} = \underset{\sim}{Q}.\underset{\sim}{D}.\underset{\sim}{Q}^{T} \\ \underset{\sim}{Q} \text{ such that } \dot{\underset{\sim}{Q}}^{T}.\underset{\sim}{Q} = \underset{\sim}{\Omega} \text{ (corotational)} \end{cases} \tag{1}$$

where $\underset{\sim}{\Omega}$ is the skew-symmetric part of the gradient $\underline{\underline{L}}$ of the velocity field, and $\underset{\sim}{D}$ its symmetric part (Besson et al., 2009; Sidoroff and Dogui, 2001).

The strain rate tensor $\underset{\sim}{\dot{\varepsilon}}$ is split into elastic and plastic contributions, the evolution of the latter being given by the plastic flow rule. The stress is computed from the elastic strain $\underset{\sim}{\varepsilon}_e$ through Hooke's law:

$$\underset{\sim}{\dot{\varepsilon}} = \underset{\sim}{\dot{\varepsilon}}_e + \underset{\sim}{\dot{\varepsilon}}_p, \quad \underset{\sim}{\sigma} = \underset{\approx}{\Lambda} : \underset{\sim}{\varepsilon}_e \tag{2}$$

where $\underset{\approx}{\Lambda}$ is the fourth order tensor of elastic moduli. The plastic strain is computed from the normality rule

$$\underset{\sim}{\dot{\varepsilon}}_p = \dot{p}\underset{\sim}{n}, \quad \underset{\sim}{n} = \frac{\partial f}{\partial \underset{\sim}{\sigma}} \tag{3}$$

and the equivalent plastic strain rate $\dot{p}$ obeys a thermal activation law defined as:

$$\dot{p} = \dot{p}_0 \sinh\left(\frac{\langle f \rangle}{K}\right) \tag{4}$$

The function f in Eq. (3) is the yield function which is based on a Hosford criterion (Hosford, 1972) with isotropic hardening:

$$f(\underset{\sim}{\sigma}, \rho, t_a) = \sigma_{eq}(\underset{\sim}{\sigma}) - R(\rho) - R_a(t_a) \tag{5}$$

$$R(\rho) = \sigma_0 + \alpha\mu b\sqrt{\rho}, \quad \dot{\rho} = A\left(1 - \frac{\rho}{B}\right)\dot{p}, \quad \rho(t=0) = \rho_0 \tag{6}$$

where $\sigma_{eq}(\underset{\sim}{\sigma})$ is the Hosford equivalent stress.

$$\sigma_{eq} = \left[\frac{(\sigma_I - \sigma_{II})^m + (\sigma_{II} - \sigma_{III})^m + (\sigma_I - \sigma_{III})^m}{2}\right]^{1/m} \tag{7}$$

where $\sigma_I > \sigma_{II} > \sigma_{III}$ are the eigen-values of the stress tensor.

The parameter m in this equivalent stress definition can be chosen to describe either von Mises surface ($m=2$ or $m=4$), either Tresca one ($m=1$ or $m=\infty$), or intermediate surfaces. The

Table 1
Constitutive parameters describing elasticity, plasticity, hardening and ageing.

E (GPa)	ν	m	σ_0 (MPa)	α	A (m^{-2})	B (m^{-2})	P_1 (MPa)	t_0 (s)	n	w
210	0.3	20	185	0.35	8.92×10^{15}	1.6×10^{15}	175	10^{30}	0.06	5×10^{-4}

dislocation density ρ is introduced in the model with the initial value $\rho_0 = 10^{-13}\mathrm{m}^{-2}$. The classical strain hardening is given by the term $R(\rho)$ which follows the evolution law defined in Eq. (6), the multiplication and dynamic recovery parameters characterizing the dislocation evolution law being A and B, respectively. The dislocation density evolution rule is driven by the cumulative plastic strain rate $\dot{p}$, as done for instance in Fressengeas et al. (2005). The yield stress $R_0 = \sigma_0 + \alpha\mu\sqrt{\rho_0}$ is the "virtual" initial yield stress that would be measured in the same steel in the absence of static strain ageing.

The second contribution to the yield stress, $R_a(t_a)$, is due to strain ageing, following Zhang et al. (2001), Graff et al. (2004), Mazière et al. (2010) and Klusemann et al. (2015). It depends on an additional internal variable t_a called the ageing time, and takes the form

$$R_a(t_a) = P_1 C_s(t_a), \quad \text{with} \quad C_s = 1 - \exp\left[-\left(\frac{t_a}{t_0}\right)^n\right] \tag{8}$$

$$\dot{t}_a = 1 - \frac{t_a \dot{p}}{\omega}, \quad t_a(t=0) = t_{a0} \tag{9}$$

The strain ageing term R_a is proportional to the variable C_s that is related to the over–concentration of solute atoms around pinned dislocations. This variable increases with the ageing time t_a, the condition corresponding to fully pinned dislocations being given by $C_s = 1$. The unpinned state corresponds to $C_s = 0$. The parameter P_1 corresponds to the maximal additional stress needed to switch from unpinned to pinned states. The parameter t_0 and the power n control the kinetics of the pinning and unpinning processes. Another parameter labeled ω appears in the evolution law of the ageing time. It is related to the incremental strain resulting from the freeing of unpinned dislocations. The inital pinning is driven by the initial values if the ageing time t_{a0}. In this study a fully anchored initial state is assumed, taking $t_{a0} = 10^{30}$s.

3.2. Identification of material parameters

The identification of this model was carried out using the tensile experiment as described in Marais et al. (2012). In the absence of tensile tests at different strain rates, the values of the parameters in the flow rule Eq. (4) are directly taken from the latter article: $K = 2.55$ MPa and $\dot{p}_0 = 3.5 \times 10^{-10}\mathrm{s}^{-1}$. These values lead to almost no strain rate sensitivity, which is generally the case at room temperature for such steels. The identification procedure which takes into account the characteristics of the Lüders phenomenon is not recalled. The parameters are given in Table 1.

The experimental evolution of the shear stress as a function of shear strain is plotted on Fig. 4 together with the corresponding model response for different values of the Hosford parameter m. It can be seen that the von Mises criterion (i.e. $m = 4$) overestimates the shear stress level, while an accurate prediction of the post-Lüders behavior is obtained for $m = 20$. This value is then used in all the simulations presented in the following. It can also be seen from Fig. 4 that the stress peak level for the shear test is inaccurately described for all values of the Hosford parameter. The amplitude of the peak stress was accurately identified for the tensile test. The one predicted for the shear stress is overestimated. This is probably due to the imperfect experimental boundary conditions compared with the simulated ones.

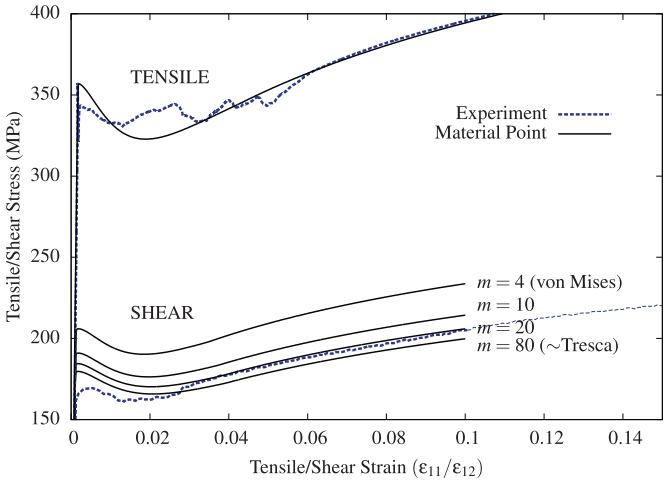

Fig. 4. Experimental shear and tensile curves and the corresponding model responses on a material point for different levels of the Hosford parameter m. The experimental curve is a global stress (force divided by the section) vs. strain (relative displacement divided by the gauge length) response of the shear specimen, while the simulated ones (denoted material point) are the local responses of the material behaviour to pure tensile and pure shear loadings. The adequate value $m = 20$ corresponds to an equivalent stress measure close to Tresca equivalent stress.

This set of parameters is used to simulate the response of the whole tensile specimen by the finite element model. A two-dimensional simulation has been carried out using the finite element software Zset (Besson and Foerch, 1997; Z–set package, 2013). The global size of the considered dogbone tensile specimen under plane stress conditions is 64 mm length and 14 mm width. The gauge length area has 36 mm length and 6 mm width. The specimen is meshed using 8 node quadratic elements with reduced integration.

It can be seen on Fig. 5 that the main features of the Lüders phenomenon (yield peak level, length and level of the plateau,...) are correctly described by the finite element simulation. However a small difference with the experimental curve appears just after the yield peak. This part of the stress strain curve (i.e. when the finite element curve departs from the material point one) corresponds to the nucleation of the Lüders band and is highly dependent on the experimental conditions such as the alignment of the testing device. Because of imperfect experimental conditions the nucleation usually occurs quite early, i.e. at yield peak. On the contrary, due to perfect boundary conditions in the finite element model, the nucleation occurs approximately at 0.5% strain after the yield peak.

4. Numerical simulations of shear tests

The material model identified in Section 3.2 is used in the present section to simulate the shear test presented in Section 2. The mesh sensitivity of the finite element simulations is firstly investigated. A strain gradient plasticity modified model is then proposed to overcome the found mesh–dependence, calibrated, and used for the full simulation of the shear experiment.

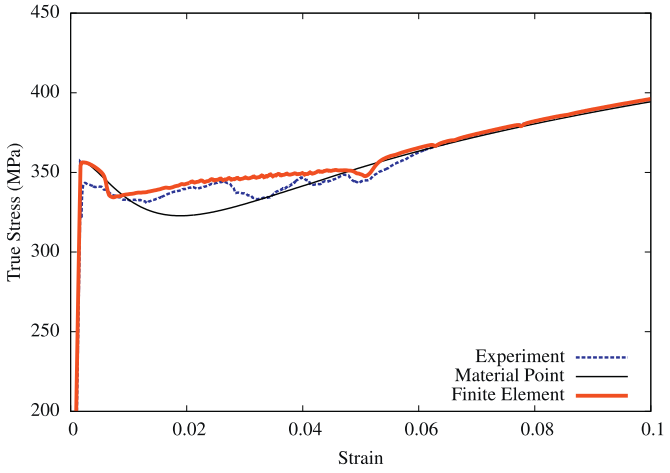

Fig. 5. Experimental tensile stress vs. strain curve and the corresponding simulated response on a material point and on a finite element plate. The Lüders plateau (and the associated propagation of a plastic band) occurs in the finite element plate simulation and in the experiment. In the finite element results, an increasing stress is found instead of a plateau. This is due to the fact that the true stress is plotted instead of the engineering one. The latter would give a flat plateau.

4.1. Mesh sensitivity evidence

The mesh sensitivity of the finite element simulations of Lüders band formation and propagation under shear testing conditions is along the following guidelines:

- It is well–known that 2D finite element simulations promote artificially strain localisation and mesh sensitivity of the results. 3D simulations on very thin geometries also are in general mesh sensitive (see Mazière and Forest (2015) for more details). In the present section, finite element simulations are consequently carried out on 3D meshes of rather thick plates (0.5 mm) with enough elements in the thickness (2 to 8). This thickness differs from the experimental one for the purpose of illustration.
- A mesh sensitivity analysis is valid if carried out on sufficiently fine meshes and on a large enough range of element sizes. Four different element sizes are used in this study, the number of integration points in the thickness of the plate varying from 4 to 16, the element size from 0.25 to 0.0625 mm.
- The element type is known to influence the strain localisation phenomena. In particular when a regular mesh whose elements are aligned with the most favourable stain localisation direction – 0/90° for shear test – is used. Two types of meshes are used in this study – free (randomly distributed) and regular – with reduced integration quadratic elements.

The 8 meshes used for this study are plotted in Fig. 6. The boundary conditions are such that the bottom surface is clamped, while the top surface is fixed along X_1 direction and homogeneously displaced along X_2 direction to apply the shear loading (see Fig. 6 for the definition of the coordinate axes).

Fig. 7 summarizes the results obtained for the finite element simulations on regular meshes. On the top figure the shear stress/strain evolution is plotted for the different meshes. Some oscillations appear for the finer meshes with an apparent link between the oscillation period and the mesh size. This phenomenon was related in some previous articles (Ballarin et al., 2009; Marais et al., 2012; Mazière and Forest, 2015) –for tensile loadings only– to a mesh dependency of the results. It must be noted that the well known localisation analysis proposed by Rice (1976), predicts a preferential angle for the localisation of bands of ± 45° in the

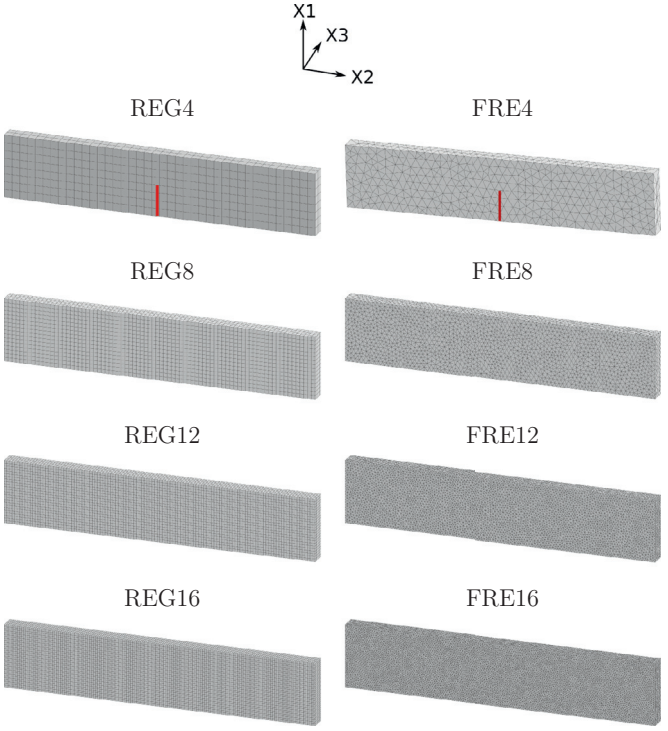

Fig. 6. Orientation of the coordinate axes and the 8 different meshes (4 free and 4 regular) used for the mesh sensitivity analysis the shear test. The specimen size is 10 mm × 2 mm × 0.5 mm.

principal stresses frame. It means that the regular elements used are then aligned with this favourable direction and localisation phenomena should be promoted.

In the middle picture of Fig. 7, the evolution of the shear strain ε_{12} is plotted for the 4 different regular meshes along a line parallel to X_1 axis at the centre of the specimen (see the meshes REG4 and FRE4 in Fig. 6 for the location of this line). These profiles are plotted at a strain level corresponding to point **C** on the shear stress vs. strain curve. For all meshes it can be observed that the band front –the transition area between the plastically deformed and the undeformed material– is located between two consecutive integration points. The band front width is then equal to the distance between two integration points: 0.125 mm for REG4 mesh, 0.0625 mm for REG8 mesh, etc. These results are in agreement with previous observations in tension made by Marais et al. (2012).

The bottom picture of Fig. 7 gives the plot of the derivative of the shear strain component ε_{12} with respect to X_1 coordinate. It appears again that the band front is systematically distributed on both sides of one single integration point. The maximum value of this gradient component increases almost linearly with the inverse of the element size.

The same three pictures are plotted on Fig. 8 for the simulations carried out on the 4 different free meshes. The oscillations during the Lüders plateau are no longer observed on the stress vs. strain curves. The evolution of the shear strain ε_{12} along X_1 is smoother than for the corresponding regular meshes. The convergence of the results is reached for the two finest meshes in most places of the sample, except within the band front zone. The band front thickness becomes smaller and smaller when the element size decreases. It is even more visible in the plot of the strain gradient component (bottom figure) where the maximal value increases quasi–linearly with the inverse of the element size.

The maps of the shear strain ε_{12} are plotted for the 4 regular meshes and the 4 free meshes on Fig. 9 for a strain level corresponding to point **C**. The main bands aligned with the horizontal

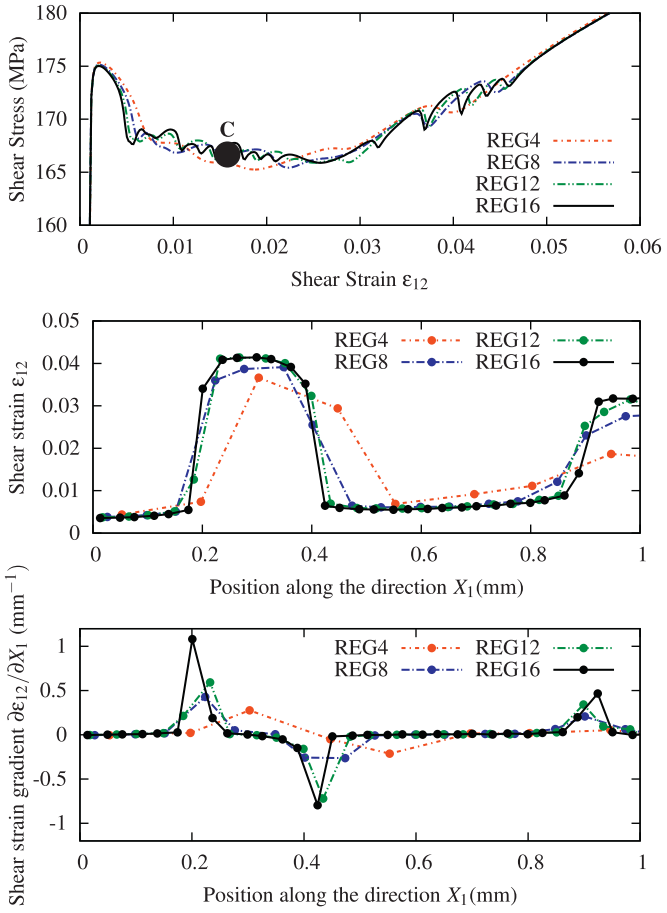

Fig. 7. (top) Global shear stress vs. strain finite element curves for the 4 3D regular meshes of Fig. 6. (center) Evolution of the shear strain ε_{12} along a line oriented in the X_1 direction at the centre of the specimen for a given global deformation corresponding to point **C**. (bottom) Evolution of the gradient of the shear strain with respect to X_1 coordinate $\partial\varepsilon_{12}/\partial X_1$ (mm^{-1}) along the same line at the same point **C**.

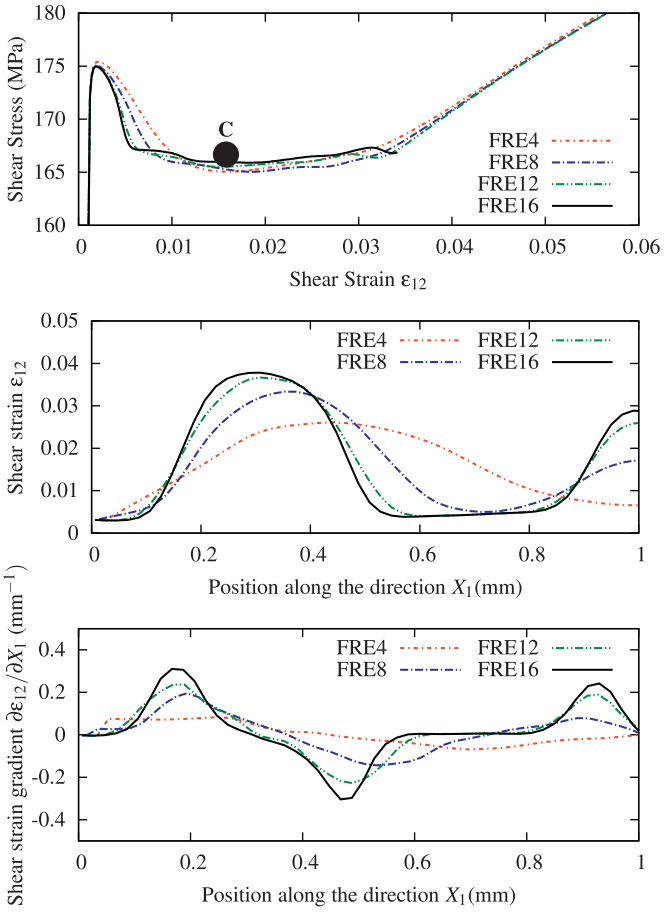

Fig. 8. (top) Global shear stress vs. strain finite element curves for the 4 3D free meshes of Fig. 6. (center) Evolution of the shear strain ε_{12} along a line oriented along X_1 at the centre of the specimen for a given global deformation corresponding to point **C**. (bottom) Evolution of the gradient of the shear strain with respect to X_1 coordinate $\partial\varepsilon_{12}/\partial X_1$ (mm^{-1}) along the same line at the same point.

X_2 direction are accompanied by several secondary bands aligned along X_1 in the case of regular meshes. These bands appear mainly far from the center of the specimen due to boundary layer effects associated with left and right free surfaces. The vertical and horizontal orientations for bands are in agreement with the localisation analysis by Rice and were also observed in former studies on the simulation of Portevin - Le Chatelier effect during shearing of square plates (Graff et al., 2008; Mazière, 2007). In contrast, such secondary bands are not observed in the simulations carried out on the free meshes.

Based on the analysis presented in this section, the following conclusions can be proposed about the mesh sensitivity of finite element simulations of the Lüders band propagation under shear:

- The yield peak and the average level of the plateau are two mesh–independent quantities.
- The evolution of the stress on the Lüders plateau is almost mesh insensitive provided that a free mesh is used. If a regular mesh is used with elements aligned along the most favourable localisation direction, serrations appear along the plateau with a frequency proportional to the inverse of the element size. This is due to the fact that in this case the problem becomes a quadi–1D deformation problem, and that the band propagates step by step controlled by the element boundary.
- For any given strain level selected during the band propagation (i.e. in the middle part of the plateau), the evolution of the shear strain in the band front region is mesh–dependent for any type of mesh. The band front width is linearly proportional to the inverse of the element size and can be estimated to about 1 element for the regular meshes and to about 2 elements for the free meshes.

Taking into accound the fact that the viscosity parameters are fixed in the analysis, a regularisation procedure using a strain gradient plasticity model is then required to overcome the latter mesh dependence.

4.2. Strain gradient plasticity model and simulations

The classical non regularized model is the previous elastoviscoplastic material behaviour characterized by the tensor of elastic moduli $\underset{\approx}{\boldsymbol{\Lambda}}$, the non-linear hardening variable $R(\rho)$, the strain-ageing hardening $R_a(t_a)$ and the flow rule. In the micromorphic extension of this model, a new degree of freedom, p_χ is introduced which has the physical meaning of a plastic microdeformation (see Forest (2009) for a more detailed presentation of the model). It has to be compared to the accumulative plastic strain p. Under homogeneous loading conditions, we have $p_\chi = p$, whereas the plastic microdeformation can differ from p in the presence of strain gradients. Two additional material parameters are introduced, namely, the coupling modulus H_χ (unit MPa) and the second rank tensor of higher order moduli $\underset{\sim}{\boldsymbol{A}}$ (unit MPa.m^2).

$$\underset{\sim}{\sigma} = \underset{\approx}{\boldsymbol{\Lambda}} : \underset{\sim}{\varepsilon^e} \tag{10}$$

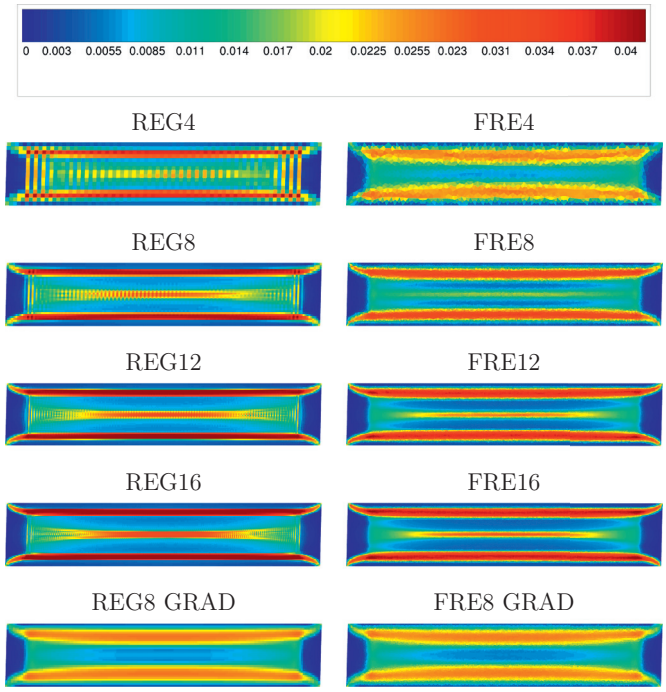

Fig. 9. Maps of shear deformation ε_{12} at a strain level corresponding to point **C** for the 8 3D simulation carried out using the 4 regular and 4 free meshes of Fig. 6. For comparison, the same maps are plotted at the bottom for the strain gradient model using the meshes REG8 and FRE8 and the value of the internal length $l_c = 0.35$ mm identified in Section 4.2.

$$a = -H_\chi (p - p_\chi) \tag{11}$$

$$\underline{\boldsymbol{b}} = \underset{\sim}{A}.\nabla p_\chi \tag{12}$$

$$R = R(\rho) + H_\chi (p - p_\chi) \tag{13}$$

where a and $\underline{\boldsymbol{b}}$ represent generalized stresses conjugate to the plastic microdeformation and its gradient, respectively, in the generalized work of internal forces. The classical and generalized stress tensors must fulfill two balance equations in the form of divergence equations:

$$\mathrm{div}\, \underline{\sigma} = 0, \quad \mathrm{div}\, \underline{\boldsymbol{b}} - a = 0 \tag{14}$$

in the absence of body forces and in the static case.

When inserted in the additional balance equation $(14)_2$, the state laws lead to the following partial differential equation

$$p_\chi - \frac{1}{H_\chi} \mathrm{div}(\underset{\sim}{A}.\nabla p_\chi) = p \tag{15}$$

Let us specialize this equation to the case of isotropic materials, for which the second order tensor of micromorphic stiffness reduces to $\underset{\sim}{A} = A\underset{\sim}{1}$ which involves a single additional material parameter. Eq. (15) then becomes

$$p_\chi - l_c^2 \Delta p_\chi = p, \quad \text{with} \quad l_c^2 = \frac{A}{H_\chi} \tag{16}$$

where l_c is the characteristic length of the model.

As a result, the hardening function can also be written

$$R = R(\rho) - A\Delta p_\chi \tag{17}$$

The material parameter H_χ can also be seen as a penalty coefficient that forces the relative plastic strain $e = p - p_\chi$ to remain small. It can be shown that a high value of H_χ keeps e close to zero. In that case, the plastic microdeformation p_χ in the hardening law (17) can be replaced by p itself:

$$R = R(\rho) - A\Delta p \tag{18}$$

which is exactly Aifantis strain gradient plasticity model with $R(\rho)$ instead of $R(p)$. In that case, there is one single new material parameter, namely A. In the following, a high enough value of H_χ is fixed at 10^4, and the value of the characteristic length l_c (or indirectly of parameter A) must be identified.

The question of parameter identification from strain field measurements for nonlinear models is still open. Various cost functions have been proposed including average or local values. The question is all the more important for strain gradient models since inhomogeneous strain fields are necessary for their calibration. This has been discussed for instance by Geers et al. (1998). In the case of plastic strain localization, the localization band width is the usual local quantity used for the identification of the internal length (see Forest et al., 2005; Mühlhaus and Vardoulakis, 1987). For a propagating band, the band width is not characteristic of the internal length. Instead, the diffuse band front is thought to be the most sensitive zone for strain gradient parameter identification. The maximum plastic strain gradient value is reached inside the band front and is a good candidate for identification. This is the choice made in the present work. It has the disadvantage that significant scatter exists for this variable when computed from the experimental data. However it will be shown that it provides an accurate estimate of the internal length. The characteristic length, l_c, can be identified using the local strain measurements given by the digital image correlation method and presented on Fig. 3. This identification is a rather long process since:

- It must be done on the full structure to evaluate the influence of l_c on the localisation pattern.
- In all the structural computations used for the identification, the mesh size must be small enough compared to l_c to ensure convergence of the solution.
- A specific variable must be chosen to compare experimental and numerical results and perform the identification. The selected variable is the maximum value of the gradient along direction X_1 of the shear strain ε_{12} for a given global deformation corresponding to point **C** (see Figs. 1,2,3,7,8).

This last quantity has been estimated from the experiments using DIC measures to be close to 0.073 mm^{-1}. In the simulations carried out using the model without strain gradient and the regular meshes (see Section 4.1 and Fig. 7), this maximum value is equal to 0.28 mm^{-1} for the coarser mesh and 1.08 mm^{-1} for the finest one. For the simulations carried out using the model without strain gradient and the free meshes (see Section 4.1 and Fig. 8), this maximum value is equal to 0.08 mm^{-1} for the coarser mesh and 0.30 mm^{-1} for the finest one. The maximal value of the gradient of ε_{12} is then in agreement with experimental value (0.073 mm^{-1}) only for the coarser free mesh.

Five different regular meshes with different element sizes have been used with the regularized micromorphic model with five different values of the internal length (25 simulations have been carried out). For a better comparison with experimental results, the whole specimen area has been meshed i.e. 30×2 mm using element sizes from 0.2 mm to 0.0125 mm. This analysis has been carried out using 2D plane stress formulation for the sake of computational efficiency. For each simulation, the maximal value of the gradient of ε_{12} was estimated for a given global deformation corresponding to point **C**. As in the experiment, this value is calculated from the evolution of ε_{12} along a vertical line located at the centre of the specimen. The evolution of this quantity with respect to the mesh size and the internal length is plotted on Fig. 10. It can be seen that:

- The micromorphic model provides indeed mesh objective results, at least if the element size is small enough and/or if the internal length is large enough;

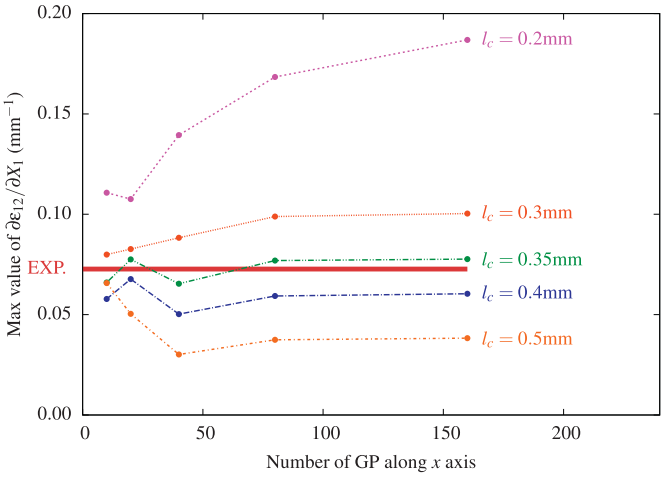

Fig. 10. Evolution of the maximum value of the gradient along direction X_1 of the shear strain ε_{12} for a given global deformation corresponding to point **C** in Figs. 7 and 8 for 5 different meshes using the micromorphic model with 5 different internal lengths. Comparison with the experimental value provided by DIC measures.

- The value $l_c = 0.35$ mm seems to be the most adequate among the values tested in order to fit the experimental field measurements.

It must be noted that the 2D simulations carried out with the strain gradient model presented in this section have been validated by a comparison with the 3D ones presented at the bottom of Fig. 9. In particular, the maximal value of the gradient of ε_{12} is not modified by changing the mesh dimension (2D/3D) and type (free or regular) but is only controlled by the value of the internal length $l_c = 0.35$ mm.

It must be outlined that the experimental value of the maximal gradient of ε_{12} at point **C** (0.073 mm^{-1}) is probably sensitive to the features of the digital image correlation process. The size of the grid used in DIC and the method used to compute ε_{12} from displacement field could lower the experimental precision on this quantity. In the present study, the maximal value of the gradient of ε_{12} is calculated from a point by point differentiation on the evolution of ε_{12} along a vertical line at the centre of the specimen as plotted on Fig. 3. Using this method, it is almost the same at points **B** and **C** (see Fig. 3). This is also the case for numerical estimates of this quantity that remain almost constant during simulations, at least in the middle part of the plateau. The maximal value of the gradient of ε_{12} can be regarded as an original and simple quantity to use for the identification of the internal length l_c. However, a more complete study on the influence of DIC features on the evaluation of this quantity would be required for a more accurate and robust identification.

The stress vs. strain curves for 2D meshes using $l_c = 0.35$ mm are plotted on Fig. 11, together with the variation of the shear strain ε_{12} along X_1 at the centre of the specimen for a given global deformation corresponding to point **C**, and the corresponding experimental and simulated (using the intermediate mesh) shear strain maps. It can be seen on the second figure that the strain evolution is no longer mesh sensitive and is very similar to the experimental one provided by DIC on Fig. 3.

However three main differences between the experiment and the simulation must be outlined:

1. The shear strain level before the band passing (i.e. in the middle area of the line along X_1) is close to 0 in the experiment while it reaches almost 0.6% in the simulation due to an initial homogeneous yielding in the specimen before or during the nucleation of the band. The shear strain level after the band passing (i.e. in the extreme area of the line along X_1) is consequently also slightly smaller in the simulation than in the experiment, since the total strain level has to be the same.
2. The yield peak and the level of the plateau are almost 10 MPa higher in the simulation than in the experiment. However, as already mentioned in Section 3.2 the strain ageing parameter controlling the Lüders peak and plateau have only been identified using the tensile experiment. The simulation of shear test is a prediction that is not adjusted afterwards.
3. The DIC image of shear strain at point **C** extracted from Fig. 2 shows a non symmetrical deformation pattern, while the corresponding simulation map drawn at the bottom of Fig. 11 is fully symmetric.

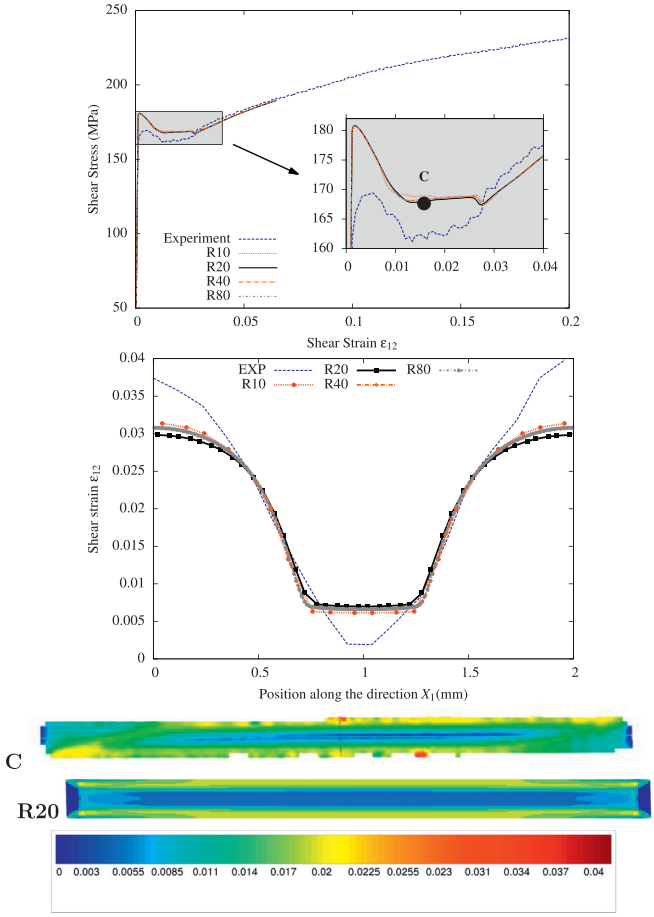

Fig. 11. Experimental shear stress vs. strain curve and the corresponding finite element curve for the 2D meshes and the micromorphic model with $l_c = 0.35$ mm. Evolution of the shear strain along a line oriented along X_1 at the centre of the specimen for a given global deformation corresponding to point **C**. Maps of the shear strain ε_{12} (blue 0%, red 5%) at the same point for the different meshes. (For interpretation of the references to colour in this figure legend, the reader is referred to the web version of this article.)

Based on these three observations another simulation is proposed in the following part introducing more realistic boundary conditions.

4.3. Influence of boundary conditions

The finite element simulations presented in Section 4.2 have been carried out assuming some perfect boundary conditions. The lower side of the $30 \times 2 \times 0.24$ mm sheared zone was assumed to remain fixed along all directions, while the upper side was shifted

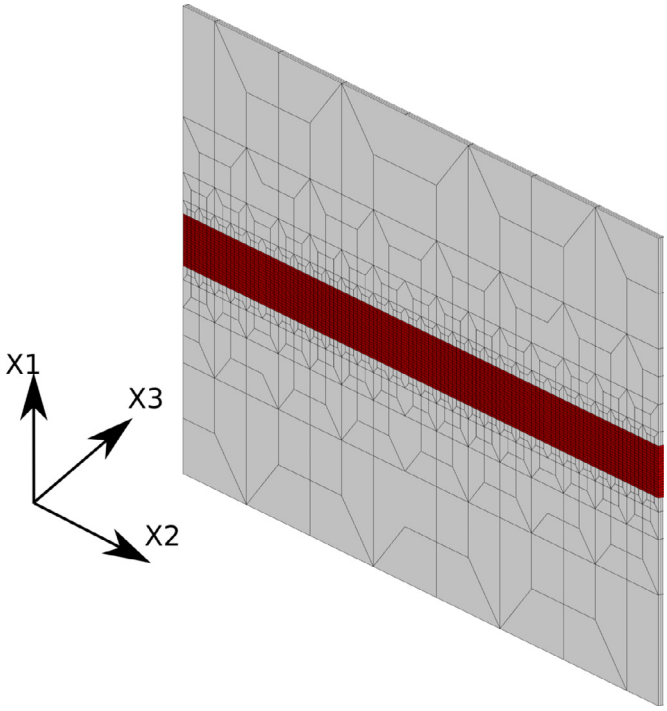

Fig. 12. Mesh used for the simulation of the shear test accounting for the grip system. The sheared zone is painted in red. (For interpretation of the references to colour in this figure legend, the reader is referred to the web version of this article.)

along the X_2 direction with a uniform translation. The influence of the grip system is consequently not accounted for using such boundary conditions. In particular, the metal sheet is compressed between grips and then deformed along X_3 direction outside the sheared zone before applying the shear displacement (Fig. 12). A simulation accounting for this deformation is proposed in this section:

- The whole $30 \times 18 \times 0.24$ mm plate is meshed using 3D 20 nodes quadratic reduced elements, with three elements in the thickness.
- The mesh is divided in 3 groups of elements, the upper grip, the lower grip, and the sheared zone.
- The loading path is prescribed in 2 stages. During the first one the upper and lower grips are compressed along X_3 direction up to 0.5% strain. During the second stage the upper grip is displaced along X_2 direction to shear the central zone of the specimen. The sample and the grips are assumed to be perfectly glued in the simulation, this latter is maybe not totally realistic especially in the corners.

The stress vs. strain curve resulting from this simulation and the corresponding map of the shear strain ε_{12} are plotted on Fig. 13. Accounting for the grips in the simulation reduces the level of the stress peak which becomes closer to the experimental one. Furthermore, the deformation map given by the simulation at point **C** does not display the previous mirror symmetry but shows a twisted pattern (point symmetry around the center) similar to the one observed using DIC. Accounting for the whole specimen and the modelling of the grip system seems to be a way of improving the simulation of the shear test in presence of a Lüders band.

5. Conclusion

The main contributions of the present work are the following:

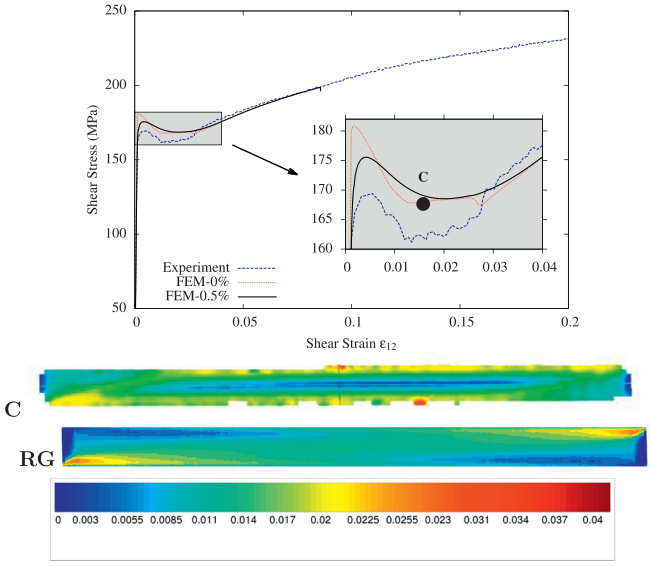

Fig. 13. Experimental shear stress vs. strain curve and the corresponding finite element curve for the 3D full mesh without (FEM-0%) and including (FEM-0.5%) grips and the micromorphic model with $l_c = 0.35$ mm. Maps of the shear strain ε_{12} (blue 0%, red 5%) for a given global deformation corresponding to point **C**. (For interpretation of the references to colour in this figure legend, the reader is referred to the web version of this article.)

1. An elastoviscoplastic model accounting for static strain ageing is identified in order to simulate the Lüders band propagation in a low carbon ferritic steel under simple tension and simple shear. The parameters of the model are identified on the tensile experiment following the procedure proposed by Marais et al. (2012). The von Mises plasticity criterion is found to be inadequate to model simultaneously the tensile and shear experiments. Instead, the Hosford equivalent stress measure was introduced in the model with an exponent m equal to 20.
2. The material model is introduced in a finite element analysis to simulate shear testing using various mesh sizes and types (free and regular), always in 3D. The global shear stress vs. shear strain curve is mesh independent for the free meshes, but slightly mesh dependent for the regular ones. On the contrary, some mesh sensitivity of Lüders band simulation in shear was evidenced for both type of mesh regarding the localization patterns and the values of shear strain gradient. In particular the band front is reduced to one or two lines of elements for all the meshes.
3. A micromorphic model is then proposed based on the introduction of an additional degree of freedom and an additional material parameter l_c called the characteristic or internal length. The micromorphic model was tested on 5 2D regular mesh for 5 different internal lengths. The determination of the suitable value for the internal length $l_c = 0.35$ mm has been carried out by a comparison with experimental results provided by DIC strain field measurements, based on the detection of the maximum shear strain gradient value.
4. A more realistic simulation of the boundary conditions has been proposed accounting for grip tightening. This modification attempts to explain the relatively small Lüders peak observed during the shear experiment and the central symmetric pattern of the deformation observed using DIC measurements.

The value of the internal length l_c has been identified using macroscopic observations. The relation to intrinsic material lengths – for example grain size – remains an open question. The value of 0.35 mm is ten times smaller than the value proposed in a former study on another ferritic steel (Marais et al., 2012). How-

ever in the present study the grain size is around $15\,\mu$m while in Marais et al. (2012) this latter is around $25\,\mu$m. Furthermore, it is derived in Mazière and Dierke (2012) that the band front width is a function of this internal length and also of the slope of the local law in the softening and hardening parts (see Fig. 5). Consequently two different internal lengths can lead to the same band front width if the local laws are also different. It would consequently be very interesting to investigate more systematically the influence of grain size and pre-straining on the Lüders band features and on l_c. Finally, the importance of proper modeling of Lüders banding phenomena under complex loading paths in steels should be underlined in particular regarding fracture processes in such industrial alloys, as illustrated in the analysis of Charpy tests by Marais et al. (2015).

Acknowledgements

The authors would like to acknowledge A. Hocini for his useful contribution during experiments involving digital image correlation.

References

Aguirre, F., Kyriakides, S., Yun, H.D., 2004. Bending of steel tubes with Lüders bands. Int. J. Plast. 20, 1199–1225.
Amar, E., Pineau, A., 1985. Interpretation of ductile fracture-toughness temperature-dependence of a low strength steel in terms of a local approach. Engng Fract. Mech. 22 (6), 1061–1071.
Ballarin, V., Perlade, A., Lemoine, X., Bouaziz, O., Forest, S., 2009. Mechanisms and modeling of bake-hardening steels: Part II. Complex loading paths. Metall. Mater. Trans. A 40, 1375–1384.
Belotteau, J., Berdin, C., Forest, S., Parrot, A., Prioul, C., 2009. Mechanical behavior and crack tip plasticity of a strain aging sensitive steel. Mater. Sci. Eng. A 526 (1-2), 156–165.
Bertram, A., 2005. Elasticity and Plasticity of Large Deformations. Springer.
Besson, J., Cailletaud, G., Chaboche, J.-L., Forest, S., 2009. Non Linear Mechanics of Materials. Springer.
Besson, J., Foerch, R., 1997. Large scale object-oriented finite element code design. Comp. Meth. Appl. Mech. Engng 142, 165–187.
Bouvier, S., Haddadi, H., Levee, P., Teodosiu, C., 2006. Simple shear tests: experimental techniques and characterization of the plastic anisotropy of rolled sheets at large strains. J. Mater. Process. Technol. 172 (1), 96–103.
Coer, J., Manach, P.Y., Laurent, H., Oliveira, M.C., Menezes, L.F., 2013. Piobert-Luders plateau and Portevin-Le Chatelier effect in an Al-Mg alloy in simple shear. Mech. Res. Commun. 48, 1–7.
Cottrell, A.H., Bilby, B.A., 1949. Dislocation theory of yielding and strain ageing of iron. Proc. Phys. Soc. A62 (1), 49–62.
Elliot, R.A., Orowan, E., Udoguchi, T., Argon, A.S., 2004. Absence of yield points in iron on strain reversal after aging, and the Bauschinger overshoot. Mech. of Mater. 36, 1143–1153.
Forest, S., 2009. Micromorphic approach for gradient elasticity, viscoplasticity, and damage. Eng. Mech. 135 (3), 117–131.
Forest, S., Blazy, J., Chastel, Y., Moussy, F., 2005. Continuum modelling of strain localization phenomena in metallic foams. J. Mater. Sci. 40, 5903–5910.
Fressengeas, C., Beaudoin, A., Lebyodkin, M., Kubin, L., Estrin, Y., 2005. Dynamic strain aging: a coupled dislocation-solute dynamic model. Mat. Sci. and Eng. 51, 226–230.
Geers, M., Borst, R.d., Brekelmans, W., Peerlings, R., 1998. On the use of local strain fields for the determination of the intrinsic length scale. J. Phys. IV 8, Pr8–167–174.
Graff, S., Dierke, H., Forest, S., Neuhäuser, H., Strudel, J.-L., 2008. Finite element simulations of the Portevin - Le Chatelier effect in metal-matrix composites. Philos. Mag. 88, 3389–3414.
Graff, S., Forest, S., Strudel, J.-L., Prioul, C., Pilvin, P., Béchade, J.-L., 2004. Strain localization phenomena associated with static and dynamic strain ageing in notched specimen:experiments and finite element simulations. Mat. Sci. Eng. 387, 181–185.
Hallai, J., Kyriakides, S., 2011. On the effect of Lüders bands on the bending of steel tubes. Part I: Experiments. Int. J. Solids Struct. 48, 3275–3284.
Hallai, J., Kyriakides, S., 2011. On the effect of Lüders bands on the bending of steel tubes. Part II: analysis. Int. J. Solids Struct. 48, 3285–3298.
Hallai, J., Kyriakides, S., 2013. Underlying material response for Lüders-like instabilities. Int. J. Plast. 47, 1–12.
Hosford, W., 1972. A generalized isotropic yield criterion. J. Appl. Mech. 39, 607–609.
Johnson, G.R., Cook, W.H., 1985. Fracture characteristics of three metals subjected to various strains, strain rates, temperatures and pressures. Eng. Fract. Mech. 21 (1), 31–48.
Klusemann, B., Fischer, G., Boehlke, T., Svendsen, B., 2015. Thermomechanical characterization of Portevin-Le Chatelier bands in AlMg3 (AA5754) and modeling based on a modified Estrin-McCormick approach. Int. J. Plast. 67, 192–216.
Kubin, L.P., Estrin, Y., 1985. The Portevin-Le Chatelier effect in deformation with constant stress rate. Acta Metall. 33, 397–407.
Kyriakides, S., Miller, J.E., 2000. On the propagation of Lüders bands in steel strips. J. Applied Mech. 67, 645–654.
Kyriakides, S., Ok, A., Corona, E., 2008. Localization and propagation of curvature under pure bending in steel tubes with Luders bands. Int. J. Solids Struct. 45 (10), 3074–3087.
Liu, Y., Kyriakides, S., Hallai, J.F., 2015. Reeling of pipe with Lüders bands. Int. J. Solids Struct. 72, 11–25.
Lomer, W.M., 1952. The yield phenomenon in polycrystalline mild steel. J. Mech. Phys. Solids 1, 64–73.
Lüders, W., 1860. Über die Äusserung der Elasticität an stahlartigen Eisenstäben und Stahlstäben, und über eine beim Biegen solcher Stäbe beobachtete Molecularbewegung. Dinglers Polytech J5, 18–22.
Luis, C., 2011. Effet du temper-rolling et du vieillissement sur le comportement mécanique en trajets séquencés d'aciers ferritiques bas carbone pour l'emballage. Université Paris 13. Ph.D. thesis
Luis, C., Gasperini, M., Bouvier, S., Li, J.J., 2009. Effect of temper rolling on the mechanical behaviour of thin steel sheets under monotonous and reverse simple shear tests. Int. J. Mater. Forming 2 (1), 471–474.
Manach, P.Y., Thuillier, S., Yoon, J.W., Coer, J., Laurent, H., 2014. Kinematics of Portevin-Le Chatelier bands in simple shear. Int. J. Plast. 58 (SI), 66–83.
Marais, A., Mazière, M., Forest, S., Parrot, A., Delliou, P.L., 2015. Influence of static strain aging on the cleavage fracture of a C-Mn steel. Eng. Fract. Mech. 141 (0), 95–110.
Marais, A., Mazière, M., Forest, S., Parrot, A., Le Delliou, P., 2012. Identification of a strain-aging model accounting for Lüders behavior in a C-Mn steel. Philos. Mag. 92 (28–30), 3589–3617.
Mazière, M., 2007. Overspeed Burst of Turboengine Disks. Mines Paris - ParisTech. Ph.D. thesis
Mazière, M., Besson, J., Forest, S., Tanguy, B., Chalons, H., Vogel, F., 2010. Numerical aspects in the finite element simulation of the Portevin-Le Chatelier effect. Comp. Meth. Appl. Mech. Engng 199, 734–754.
Mazière, M., Dierke, H., 2012. Investigations on the Portevin Le Chatelier critical strain in an aluminum alloy. Comput. Mater. Sci. 52 (1), 68–72.
Mazière, M., Forest, S., 2015. Strain gradient plasticity modeling and finite element simulation of Lüders band formation and propagation. Continuum Mech. Thermodyn. 27 (1–2), 83–104.
McCormick, P.G., 1988. Theory of flow localization due to dynamic strain ageing. Acta Metall. 36, 3061–3067.
Mühlhaus, H., Vardoulakis, I., 1987. The thickness of shear bands in granular materials. Géotechnique 37, 271–283.
Nogueira de Codes, R., Hopperstad, O.S., Engler, O., Lademo, O., Embury, J., Benallal, A., 2011. Spatial and temporal characteristics of propagating deformation bands in AA5182 alloy at room temperature. Metall. Mater. Trans. A 42, 3358–3369.
Piobert, G., 1842. Expérience sur la pénétration des projectiles dans le fer forgé. Mémoire de l'Artillerie 505.
Rabahallah, M., Balan, T., Bouvier, S., Bacroix, B., Barlat, F., Chung, K., Teodosiu, C., 2009. Parameter identification of advanced plastic strain rate potentials and impact on plastic anisotropy prediction. Int. J. Plast. 25 (3), 491–512.
Rice, J., 1976. The localisation of plastic deformation. In: Koiter, W. (Ed.), Proc. 14th Int. Conf. Theoretical and Applied Mechanics, Delft. North–Holland, Amsterdam, pp. 207–220.
Sidoroff, F., Dogui, A., 2001. Some issues about anisotropic elasticplastic models at finite strain. Int. J. Solids Struct. 38, 9569–9578.
Wang, H., Berdin, C., Mazière, M., Forest, S., Prioul, C., Parrot, A., Le-Delliou, P., 2012. Experimental and numerical study of dynamic strain ageing and its relation to ductile fracture of a c-mn steel. Mater. Sc. Eng. A 547, 19–31.
Wattrisse, B., Chrysochoos, A., Muracciole, J.M., Nemoz-Gaillard, M., 2001. Kinematic manifestations of localisation phenomena in steels by digital image correlation. Eur. J. Mech., A/Solids 20, 189–211.
Wenman, M.R., Chard-Tuckey, P.R., 2010. Modelling and experimental characterisation of the Lüders strain in complex loaded ferritic steel compact tension specimens. Int. J. Plast. 26, 1013–1028.
Z–set package, 2013. Non-linear Material & Structure Analysis Suite. www.zset-software.com
Zhang, J., Jiang, Y., 2005. Lüders bands propagation of 1045 steel under multiaxial stress state. Int. J. Plast. 21, 651–670.
Zhang, S., McCormick, P., Estrin, Y., 2001. The morphology of Portevin- Le Chatelier bands: finite element simulation for Al-Mg-Si. Acta Mater. 49, 1087–1094.